ChemComm

COMMUNICATION

View Article Online
View Journal | View Issue

Check for updates

Cite this: *Chem. Commun.*, 2024, **60**, 8728

Received 23rd June 2024,
Accepted 19th July 2024

DOI: 10.1039/d4cc03051f

rsc.li/chemcomm

Published on 22 2024. Downloaded on 2025/11/8 19:22:51.

Phosphorus-doped $Ti_3C_2T_x$ MXene nanosheets enabling ambient NH_3 synthesis with high current densities†

Yuchuan Qi,‡[a] Xianghua Hou,‡[a] Ziying He,*[b] Fan He,[a] Tianran Wei,[bc] Ge Meng,*[ab] Huihui Hu,[c] Qian Liu,[d] Guangzhi Hu [e] and Xijun Liu *[c]

Herein, we show that P-doped $Ti_3C_2T_x$ MXene nanosheets can effectively catalyze the NO_3RR-to-NH_3 conversion with a high faradaic efficiency of 95% and a yield rate of 5.39 mg h^{-1} $mg_{cat.}^{-1}$. Moreover, the catalyst achieves an impressive high current density of −1200 mA cm^{-2} at a low potential of −1.51 V, accompanied by an NH_3 productivity of 123.5 mg h^{-1} $mg_{cat.}^{-1}$. Theoretical calculations further reveal that phosphorous dopants facilitate the adsorption and activation of reactants/intermediates and thus lower the energy barrier.

NH_3 assumes a significant role in the nitrogen cycle and represents a pivotal compound in fertilizers, explosives, plastics, and so on.[1–3] Generally, its industrial production strongly relies on the Haber–Bosch approach,[4,5] leading to great energy consumption and greenhouse gas emissions. In this case, NH_3 synthesized by the N_2 reduction reaction (NRR) under ambient conditions has gained much attention in recent years.[6,7] However, the poor solubility and inert chemical reactivity of N_2 molecules typically contribute to unsatisfactory selectivity and NH_3 yield rates. Therefore, the development of more efficient electrocatalytic systems is highly desirable.

More recently, the nitrate reduction reaction (NO_3RR) demonstrates advancement as compared to the NRR because of its low N═O cracking energy and good solubility,[8,9] therefore endowing NH_3 synthesis with a fast reaction rate. Besides, the NO_3RR can also alleviate the ever-increasing NO_3^- pollution in water.[10–12] In this regard, the NO_3RR acts as a dual-purpose strategy. To date, considerable efforts have been devoted to designing high-performance NO_3RR catalysts, such as RuO_x,[13] CuO_x,[14] CoO_x,[15] and single-atom materials.[16] However, these catalysts typically deliver small current densities (<100 mA cm^{-2}), indicative of low yield rates. That is, the industrial application of the NO_3RR cannot be technically achieved. Hence, the NO_3RR-to-NH_3 conversion under large current densities is still a longstanding and challenging task.

The $Ti_3C_2T_x$ MXene is exactly considered a promising catalyst for various electrochemical reactions due to its large exposure area, high conductivity, and tunable surface chemistry.[17–19] Current reports have proved that $Ti_3C_2T_x$-based catalysts can efficiently catalyze nitrate reduction to yield NH_3 with high faradaic efficiencies (FEs > 80%).[20–22] However, the obtained current densities are limited, and further improvement is needed. In this context, we introduced a phosphorus element into the $Ti_3C_2T_x$ MXene (namely P-$Ti_3C_2T_x$) to realize high-performance NO_3RR-to-NH_3 conversion, which showed a maximal FE of 95% and a corresponding yield rate of 5.39 mg h^{-1} $mg_{cat.}^{-1}$ at a potential of −1.2 V *versus* reversible hydrogen electrode (*vs.* RHE). Besides, the catalyst exhibited a stable activity over 6 cycles and 40-h long-term electrolysis. Impressively, when examined in a flow cell, the catalyst delivered a notable high current density of −1200 mA cm^{-2} at a low potential of −1.51 V *vs.* RHE, accompanied by a yield rate of 123.5 mg h^{-1} $mg_{cat.}^{-1}$, implying the potential application for NH_3 synthesis. Moreover, in-depth simulations revealed that the phosphorus dopants can dramatically optimize the reactivity of Ti sites and reduce the energy barrier, accounting for excellent NO_3RR performance.

The synthetic procedure is illustrated in Fig. 1a, where the Ti_3AlC_2 raw materials were first etched using a mixture of LiF and HCl, and then the residue was further annealed in the presence of NaH_2PO_2 to generate P-$Ti_3C_2T_x$. The representative scanning electron microscopy (SEM) images of $Ti_3C_2T_x$ and

[a] *Key Laboratory of Carbon Materials of Zhejiang Province, College of Chemistry and Materials Engineering, Wenzhou University, Wenzhou 325035, China. E-mail: 2021028852@gxgy.edu.cn, mengge@wzu.edu.cn*
[b] *Guangxi Vocational & Technical Institute of Industry, Nanning 530001, Guangxi, China*
[c] *MOE Key Laboratory of New Processing Technology for Nonferrous Metals and Materials, School of Resources, Environment and Materials, Guangxi University, Nanning, 530004 Guangxi, China. E-mail: xjliu@gxu.edu.cn*
[d] *Institute for Advanced Study, Chengdu University, Chengdu 610106, Sichuan, China*
[e] *School of Ecology and Environmental Science, Yunnan University, Kunming 650504, China*

† Electronic supplementary information (ESI) available. See DOI: https://doi.org/10.1039/d4cc03051f

‡ These authors contributed equally to this work.

This journal is © The Royal Society of Chemistry 2024

Published on 22 2024. Downloaded on 2025/11/8 19:22:51.

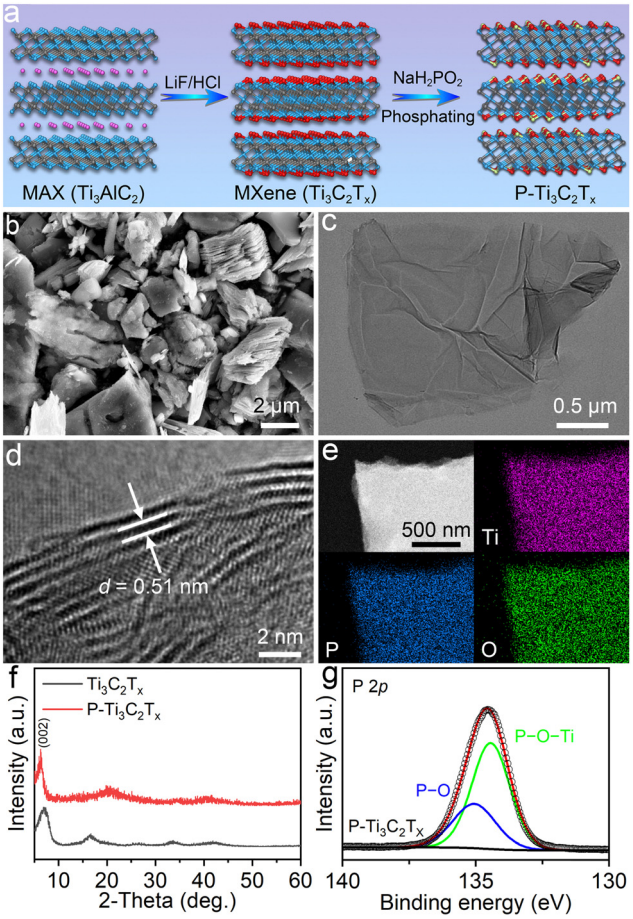

Fig. 1 (a) Schematic of the synthesis of P-$Ti_3C_2T_x$. (b)–(d) SEM, TEM and HRTEM images. (e) EDX elemental mapping images. (f) XRD patterns. (g) High-resolution P 2p XPS spectrum.

P-$Ti_3C_2T_x$ are shown in Fig. S1 (ESI†) and Fig. 1b, respectively, which clearly present sheet-like morphology, indicative of a large surface area. This favors the exposure of active sites and mass transfer during the electrolysis. The transmission electron microscopy (TEM) image in Fig. 1c confirms the multilayer lamellar structure. The high-resolution TEM (HRTEM) image reveals atomic crystal fringes with a size of 0.51 nm corresponding to the (002) plane of $Ti_3C_2T_x$ (Fig. 1d). Meanwhile, the energy-dispersive X-ray (EDX) images in Fig. 1e manifest the uniform distribution of Ti, P, and O on the surface of the nanosheet.

Further, the X-ray diffraction (XRD) patterns were collected and are displayed in Fig. 1f, which show characteristic peaks of the typical $Ti_3C_2T_x$ MXene, in line with previous reports. Compared to pristine $Ti_3C_2T_x$, the (002) peak of P-$Ti_3C_2T_x$ slightly shifts to a small angle, suggesting an increased lattice spacing.[23] Moreover, applying X-ray photoelectron spectroscopy (XPS) measurements, the survey spectrum in Fig. S2 (ESI†) also revealed the presence of the P element in P-$Ti_3C_2T_x$, conforming to the results of EDX (Fig. 1e). The high-resolution P 2p spectrum (Fig. 1g) could be deconvoluted into two peaks at 134.4 and 135.1 eV, corresponding to P–O–Ti and P–O bonds, respectively.[24] Besides, as observed in the Ti 2p XPS spectrum of P-$Ti_3C_2T_x$, the peaks at 454.8, 455.7, 456.5, and 458.3 are ascribed to Ti–C, Ti^{2+}, Ti^{3+}, and Ti–O, respectively (Fig. S3, ESI†).[25] Additionally, the O 1s XPS spectrum was deconvoluted into three peaks (Fig. S4, ESI†), which are interpreted as those of Ti–O (531.7 eV), Ti–O_x (532.8 eV), and C–Ti–$(OH)_x$ (534.0 eV).[26] The results further confirm the thriving synthesis of P-$Ti_3C_2T_x$. In addition, the optimal P content in P-$Ti_3C_2T_x$ was determined to be 5.8 wt% according to the XPS results (Fig. S5, ESI†).

Next, the NO_3RR activity of the as-prepared samples was checked by using a three-electrode configuration in a neutral electrolyte (0.5 M K_2SO_4 + 0.1 M KNO_3). The optimal catalyst loading was found to be 0.15 mg cm^{-2} (Fig. S6 and S7, ESI†). The linear scanning voltammetry (LSV) curves were first studied, and the results revealed that P-$Ti_3C_2T_x$ delivers larger current densities as compared to $Ti_3C_2T_x$ (Fig. 2a). This suggests a higher NO_3RR activity on P-$Ti_3C_2T_x$. In addition, the current densities of P-$Ti_3C_2T_x$ obtained in the blank electrolyte are lower than those in NO_3^--containing electrolyte (Fig. S8, ESI†), implying that P-$Ti_3C_2T_x$ can effectively catalyze the reduction of NO_3^-.[27] The absorbance of the dilute electrolyte was measured by a reported indophenol blue method.[28,29] As a result, FEs exhibited a volcanic trend in Fig. 2b and c due to the existence of a competitive hydrogen evolution reaction (HER),[28] which achieves a maximal FE of 95% at −1.2 V *vs.* RHE, larger than that on $Ti_3C_2T_x$ (81% at −1.1 V *vs.* RHE). Meanwhile, it can be seen that the FEs for NH_3 production are above 80% over the wide potential range, which indicates that the HER is inactive. More importantly, the measured NH_3 yield rate of P-$Ti_3C_2T_x$

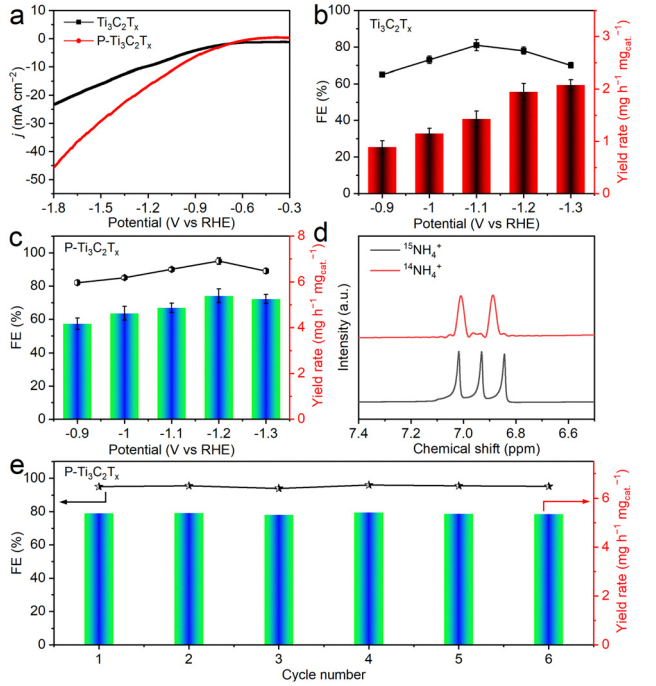

Fig. 2 (a) LSV curves in NO_3^--containing electrolytes in an H cell. (b) and (c) The obtained FEs and yield rates for $Ti_3C_2T_x$ and P-$Ti_3C_2T_x$. (d) The ^{1}H NMR spectrum. (e) Cycling stability.

Published on 22 2024. Downloaded on 2025/11/8 19:22:51.

reached 5.39 mg h^{-1} $mg_{cat.}^{-1}$, significantly higher than that of pure $Ti_3C_2T_x$ and most of the currently reported catalysts (Table S1, ESI†). When tested in a dilute electrolyte, P-$Ti_3C_2T_x$ presents the highest FE of 90% at −1.1 V *vs.* RHE (Fig. S9, ESI†).

Subsequently, the by-products of NO_2^-, N_2H_4, and H_2 are displayed in Fig. S10–S12 (ESI†), which shows that the FEs for NO_2^- and N_2H_4 are negligible, revealing the superior selectivity of NO_3RR-to-NH_3 on P-$Ti_3C_2T_x$. To verify the origin of produced NH_3, isotopic labeling tests were performed and the results are depicted in Fig. 2d, which show two characteristic peaks corresponding to $^{15}NH_4^+$, implying that the source of nitrogen in the generated NH_3 is indeed from the reduction of NO_3^-.[30] In addition, alternate electrolysis of the three-group cycles in electrolytes with and without NO_3^- confirms that NH_3 is merely produced from the NO_3RR rather than other contaminants (Fig. S13, ESI†). Fig. 2e shows multiple cycling tests at −1.2 V *vs.* RHE and no clear decay in FEs and yield rates is observed, confirming the stable electrochemical activity of P-$Ti_3C_2T_x$. Besides, the current density presented little fluctuation during the 40-h electrolysis (Fig. S14, ESI†). Furthermore, XRD patterns and SEM and TEM images manifest the robustness of P-$Ti_3C_2T_x$ (Fig. S15–S17, ESI†).

The results of double-layer capacitance demonstrated that P-$Ti_3C_2T_x$ possesses a higher active surface area compared to $Ti_3C_2T_x$ (Fig. S18, ESI†), indicative of more exposed sites for the NO_3RR. Nyquist plots further confirmed an improved efficiency for ionic transport and a low resistance for charge transfer (Fig. S19, ESI†).

The large-scale NH_3 production is vital for the commercialization of the NO_3RR.[8,31,32] In this case, we further examined the NO_3RR activity of P-$Ti_3C_2T_x$ in a flow cell and the results are depicted in Fig. 3. Clearly, P-$Ti_3C_2T_x$ drives the current densities to −1000 and −1500 mA cm^{-2} at −1.30 and −1.51 V *vs.* RHE, respectively, obviously superior to that of pure $Ti_3C_2T_x$ (Fig. 3a). The corresponding FEs at different current densities are depicted in Fig. 3b and reach the highest FE of 92% at a current density of −1000 mA cm^{-2}, and the yield rate achieves a maximum of 123.5 mg h^{-1} $mg_{cat.}^{-1}$ at −1200 mA cm^{-2} (Fig. 3c), comparable to the best results (Table S2, ESI†). Besides, the obtained yield rate at the optimal potential in a flow cell is obviously larger than that in an H cell, while the FEs are comparable (Fig. S20, ESI†).

Next, the NO_3RR stability of P-$Ti_3C_2T_x$ was assessed and the result showed that no notable discrepancy in FEs was observed after 70-h electrolysis (Fig. 3d), suggesting that P-$Ti_3C_2T_x$ is chemically stable as a catalyst during the reduction process.

To gain an in-depth insight into the NO_3RR enhancement of phosphorus-doping, density functional theory (DFT) calculations were conducted. As depicted in Fig. 4a, the introduced phosphorus facilitates the adsorption of NO_3^- (ΔE_{ab}) with a large value of −1.61 eV as compared to a pure $Ti_3C_2T_x$ surface (−1.53 eV), implying P-$Ti_3C_2T_x$ offers a strong affinity to the reactant.[33–35] The phosphorus-doping also promoted the charge transfer between NO_3^- and the catalyst surface, and the Bader analyses indicated that a charge of 0.63 e^- is transferred from P-$Ti_3C_2T_x$ to the adsorbed NO_3^- (Fig. 4b). Based on these, NO_3^- can be adsorbed and activated energetically preferred on the P-$Ti_3C_2T_x$ surface.[36]

Then, the energy barrier for the competitive HER was considered and the results are shown in Fig. 4c. As expected, P-$Ti_3C_2T_x$ had a higher H* free energy (0.14 eV) than $Ti_3C_2T_x$ (0.02 eV), indicative of the inhibition of hydrogen generation during the NO_3RR process. Moreover, the DFT results show that the potential-determining step (PDS) on P-$Ti_3C_2T_x$ corresponds to $*NO_2 + H^+ + e^- \rightarrow *NO_2H$ with an energy barrier of 1.02 eV (Fig. 4d), while after phosphorus-doping, this barrier could be greatly reduced to 0.41 eV, suggesting that dopants are responsible for the NO_3RR enhancement,[37] as revealed by the above experiments. It is also found that the subsequent elementary reactions follow a spontaneous exothermic process. Combined with experimental and theoretical analyses, we could infer that the excellent NO_3RR performance indeed originates from heteroatom doping.

In summary, P-$Ti_3C_2T_x$ proved to be an advanced NO_3RR catalyst for NH_3 synthesis under ambient conditions. In neutral media, the

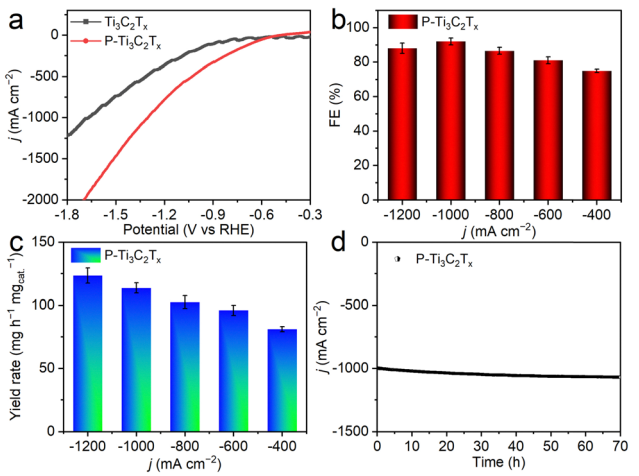

Fig. 3 (a) LSV curves in a flow cell. (b) and (c) FEs and yield rates at different current densities. (d) Stability test at −1000 mA cm^{-2}.

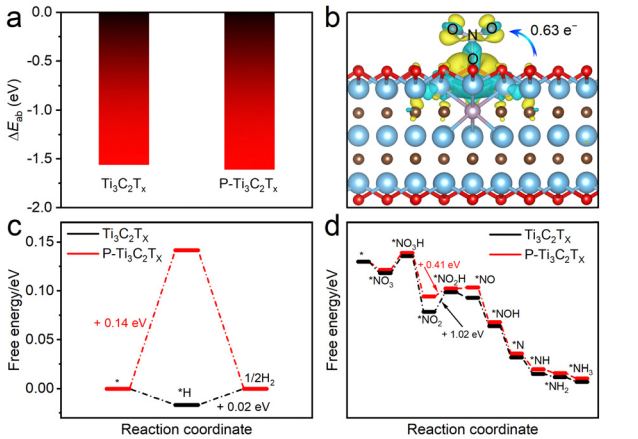

Fig. 4 (a) ΔE_{ab} of NO_3^- on the catalyst surface. (b) Charge density difference. Note that yellow and cyan shadows represent charge accumulation and depletion in the space, respectively. (c) and (d) Calculated free energy profiles for the HER and NO_3RR.

This journal is © The Royal Society of Chemistry 2024

catalyst achieved a high yield rate of 5.39 mg h^{-1} $mg_{cat.}^{-1}$ and a maximal FE of 95% with good cycling stability. More impressively, when tested in a flow cell, the catalyst delivers an ampere-level current density at a low working potential, accompanied by a high NH_3 FE, strongly suggesting the promising application in future large-scale NH_3 production. Based on the DFT studies, doping phosphorus atoms into $Ti_3C_2T_x$ can offer abundant active sites and modulate the electronic structure, efficiently promoting the adsorption and activation of reactants and intermediates and thereby lowering the NO_3RR energy barrier. In our work, an efficient catalyst is developed for the NO_3RR-to-NH_3 conversion at high current densities, which may be helpful for massive NH_3 production.

This work was financially supported by the National Natural Science Foundation of China (22109118 and 22075211).

Data availability

Data are available on request from the authors.

Conflicts of interest

There are no conflicts to declare.

Notes and references

1 N. Gruber and J. N. Galloway, *Nature*, 2008, **451**, 293.
2 M. Yang, T. Wei, J. He, Q. Liu, L. Feng, H. Li, J. Luo and X. Liu, *Nano Res.*, 2024, **17**, 1209.
3 M. Fu, Y. Mao, H. Wang, W. Luo, Y. Jiang, W. Shen, M. Li and R. He, *Chin. Chem. Lett.*, 2024, **35**, 108341.
4 L. Zhang, X.-Y. Xie, H. Wang, L. Ji, Y. Zhang, H. Chen, T. Li, Y. Luo, G. Cui and X. Sun, *Chem. Commun.*, 2019, **55**, 4627–4630.
5 X. Zou, J. Xie, C. Wang, G. Jiang, K. Tang and C. Chen, *Chin. Chem. Lett.*, 2023, **34**, 107908.
6 L. Lv, H. Tan, Y. Kong, B. Tang, Q. Ji, Y. Liu, C. Wang, Z. Zhuang, H. Wang, M. Ge, M. Fan, D. Wang and W. Yan, *Angew. Chem., Int. Ed.*, 2024, **63**, e202401943.
7 W. Qiu, S. Qin, Y. Li, N. Cao, W. Cui, Z. Zhang, Z. Zhuang, D. Wang and Y. Zhang, *Angew. Chem., Int. Ed.*, 2024, **63**, e202402684.
8 G. Zhang, G. Wang, Y. Wan, X. Liu and K. Chu, *ACS Nano*, 2023, **17**, 21328.
9 K. Chen, Z. Ma, X. Li, J. Kang, D. Ma and K. Chu, *Adv. Funct. Mater.*, 2023, **33**, 2209890.
10 J. Liang, Q. Liu, A. A. Alshehri and X. Sun, *Nano Res. Energy*, 2022, **1**, 9120010.
11 H. Yang, X. Jiang, J. Sun, B. Zhang, X. Su, Q. Wu, Z. Qu and S. Huo, *J. Alloys Compd.*, 2024, **989**, 174402.
12 H. Yang, B. Zhang, J. Sun, X. Su, S. Huo and Z. Qu, *J. Alloys Compd.*, 2024, **997**, 174956.
13 J. Li, G. Zhan, J. Yang, F. Quan, C. Mao, Y. Liu, B. Wang, F. Lei, L. Li, A. W. M. Chan, L. Xu, Y. Shi, Y. Du, W. Hao, P. K. Wong, J. Wang, S.-X. Dou, L. Zhang and J. C. Yu, *J. Am. Chem. Soc.*, 2020, **142**, 7036.
14 S. Chen, G. Qi, R. Yin, Q. Liu, L. Feng, X. Feng, G. Hu, J. Luo, X. Liu and W. Liu, *Nanoscale*, 2023, **15**, 19577.
15 N. Sun, Y. Guo, L. Luo, X. Cai, S. Shen and J. Zhang, *Appl. Surf. Sci.*, 2023, **624**, 157118.
16 W. Zhang, X. Qin, T. Wei, Q. Liu, J. Luo and X. Liu, *J. Colloid Interface Sci.*, 2023, **638**, 650–657.
17 P. Liu, P. Xiao, M. Lu, H. Wang, N. Jin and Z. Lin, *Chin. Chem. Lett.*, 2023, **34**, 107426.
18 J. Yang, F. Zhang and J. Chen, *China Powder Sci. Technol.*, 2024, **30**, 161.
19 J. Y. Loh, F. M. Yap and W.-J. Ong, *J. Mater. Sci. Technol.*, 2024, **179**, 86.
20 M. Wang, T. Hu, C. Wang, F. Du, H. Yang, W. Sun, C. Guo and C. M. Li, *Sci. China Mater.*, 2023, **66**, 2750.
21 J. Theerthagiri, J. Park, H. T. Das, N. Rahamathulla, E. S. F. Cardoso, A. P. Murthy, G. Maia, D. V. N. Vo and M. Y. Choi, *Environ. Chem. Lett.*, 2022, **20**, 2929.
22 X. Yang, G. Wei, J. Cao, Z. Ding, R. Yuan, J. Long and C. Xu, *ACS Sustainable Chem. Eng.*, 2024, **12**, 3378–3389.
23 Y. Ren, F. Tian, L. Jin, Y. Wang, J. Yang, S. You and Y. Liu, *Environ. Sci. Technol.*, 2023, **57**, 10458.
24 M. Chao, K. Zeng, C. Lu, Z. Shi, J. Guo, X. Chen and R. Yang, *J. Colloid Interface Sci.*, 2024, **657**, 46.
25 X. Liu, M. Chen, J. Ma, J. Liang, C. Li, C. Chen and H. He, *China Powder Sci. Technol.*, 2024, **30**, 35.
26 C. Kaplan, R. M. Restrepo, T. Schultz, K. Li, V. Nicolosi, N. Koch and M. P. Browne, *Electrochim. Acta*, 2024, **490**, 144269.
27 X. Hu, D. Zhou, H. Wang, W. Zhang, H. Zhong and Y. Chen, *Chin. Chem. Lett.*, 2023, **34**, 108050.
28 T. Hou, J. Ding, H. Zhang, S. Chen, Q. Liu, J. Luo and X. Liu, *Mater. Chem. Front.*, 2023, **7**, 4952.
29 X. Gao and E. C. M. Tse, *Small*, 2024, **20**, 2306311.
30 G. E. Dima, A. C. A. de Vooys and M. T. M. Koper, *J. Electroanal. Chem.*, 2003, **554–555**, 15.
31 Y. Zhao, J. Zhang, X. Guo, X. Cao, S. Wang, H. Liu and G. Wang, *Chem. Soc. Rev.*, 2023, **52**, 3215.
32 Y. Ji, Z. Yu, L. Yan and W. Song, *China Powder Sci. Technol.*, 2023, **29**, 100.
33 K. Chen, J. Xiang, Y. Guo, X. Liu, X. Li and K. Chu, *Nano Lett.*, 2024, **24**, 541.
34 M. Ghosh, M. Ibrar and J. M. Smith, *Chem. Commun.*, 2022, **58**, 4783.
35 C. Zhang, H. Xu, Y. Wang, M. An, Y. Wang, Z. Yuan, W. Zhang, C. Li, M. Guo and D. Su, *China Powder Sci. Technol.*, 2023, **29**, 80.
36 O. Q. Carvalho, R. Marks, H. K. K. Nguyen, M. E. Vitale-Sullivan, S. C. Martinez, L. Árnadóttir and K. A. Stoerzinger, *J. Am. Chem. Soc.*, 2022, **144**, 14809.
37 J. Li, S. Yan, G. Li, Y. Wang, H. Xu and G. Duan, *China Powder Sci. Technol.*, 2023, **29**, 101.

Published on 22 2024. Downloaded on 2025/11/8 19:22:51.